Article

Computational Modelling of Pyrrolic MN$_4$ Motifs Embedded in Graphene for Catalyst Design

Jian Liang Low *[ID] **and Beate Paulus** *[ID]

Institute of Chemistry and Biochemistry, Freie Universität Berlin, Arnimallee 22, 14195 Berlin, Germany
* Correspondence: low.jian.liang@fu-berlin.de (J.L.L.); b.paulus@fu-berlin.de (B.P.)

Abstract: Carbon-based materials doped with metal and nitrogen (M-N-Cs) have promising potential in electrocatalytic applications with the advantage of material sustainability. MN$_4$ motifs incorporated into a carbon lattice are generally known to be responsible for the activity of these materials. While many computational studies assume the tetrapyridinic MN$_4$ motifs, recent studies have elucidated the role of tetrapyrrolic MN$_4$ motifs in electrocatalysis. Using density functional theory, we constructed and compared various structural models to study the incorporation of tetrapyrrolic and tetrapyridinic MN$_4$ motifs in 2D carbon materials and analyzed the type of interactions between each metal species and the N$_4$ site. We further quantified the relative affinity of various metal species to the two types of N$_4$ site. Upon analysis of energies, bond lengths, electronic population and charges, we found that metals that exhibit highly ionic binding characters have a greater affinity towards tetrapyrrolic MN$_4$ motifs compared to species that participate in covalent interactions with the π-system. Furthermore, the binding strength of each species in the N$_4$ site depend on the electronegativity as well as the availability of orbitals for accepting electrons from the π-system.

Keywords: single-atom catalyst; carbon material; density functional theory; pyrrolic and pyridinic MN$_4$

1. Introduction

As humanity strives towards a sustainable economy with minimal fossil fuel combustion and carbon footprint, increasing political and economic attention has been directed towards optimizing electrochemical processes for efficient energy conversion and storage. Some of the key electrochemical processes include the oxygen reduction reaction (ORR) and carbon dioxide reduction reaction (CO$_2$RR). The former is a crucial cathodic process for energy conversion in emission-free fuel cell vehicles while the latter serves a dual purpose to control CO$_2$ emission by converting it into useful chemical products. State-of-the-art electrocatalysts for these processes are generally derived from relatively sparse elements such as the platinum group metals (PGMs) [1,2] and coinage metals [3,4], thereby posing a limit to the sustainability of these processes. Recently, electrocatalysts based on earth-abundant materials have been developed as low-cost substitutes [5–7], especially metal- and nitrogen-codoped carbon materials (M-N-Cs) which have attracted widespread attention as promising and sustainable alternatives to the PGMs [5,6].

M-N-Cs are often synthesized by pyrolyzing a combination of organic and inorganic precursors, including aromatic compounds, metal–organic frameworks, and metal salts. Due to the great degree of disorder present in the pyrolyzed materials, it is often challenging to determine the identity of active sites responsible for the catalysis, much less to understand the mechanisms behind the reactions. While there is a general agreement that the planar MN$_4$ site is the catalytically active site for most electrochemical applications [7,8], there are diverging views on how these MN$_4$ sites are incorporated into the carbon backbone. The pyridinic MN$_4$ sites are generally believed to be ideal, as their formation induces the least number of defects on the carbon backbone. However, naturally abundant MN$_4$ complexes such as haem and chlorophylls exhibit an almost exclusively tetrapyrrolic

coordination. Furthermore, various in-situ reaction studies have identified the tetrapyrrolic FeN_4 sites as the active site responsible for the high ORR activity of Fe-N-Cs [9–12].

In recent years, there have been several reports on the successful synthesis and characterization of M-N-Cs containing phase-pure tetrapyrrolic MN_4 sites [8,13]. For the synthesis of Fe-N-Cs, transmetallation strategies employing Zn as a sacrificial templating ion during pyrolysis have been developed in order to avoid side phases of iron oxides and carbides, with the identification of exclusively tetrapyrrolic sites in the synthesized material [8,14–16]. It is also worthy to note that Mg has also been employed as sacrificial templating ion [17], suggesting that the templating pathway is not exclusive to Zn. With the successful implementation of the transmetallation strategies, it is now possible to incorporate a certain level of control in the unpredictable pyrolytic synthesis. As the morphology and site density remain relatively unchanged after transmetallation, quantitative studies on the intrinsic activities of MN_4 sites could potentially be performed [18]. In addition, less conventional choices of metal dopants could in principle be introduced into the system, leading to a wide range of unexplored M-N-C catalysts. In this study, we apply density functional theory (DFT) to compare the affinity of various metals towards tetrapyrrolic and tetrapyridinic MN_4 motifs. For simplicity, since this study deals exclusively with tetracoordinated MN_4 sites, the terms tetrapyrrolic and tetrapyridinic will be shortened to pyrrolic and pyridinic, respectively.

2. Computational Details

In general, the density functional theory (DFT) calculations were performed in the unrestricted/spin-polarized Kohn–Sham formalism. The PBE functional was used for the initial comparisons between the cluster and periodic calculations [19]. For the extended study involving different metals in the MN_4 clusters, we switched to the hybrid PBE0 functional in order to reduce the delocalization error associated with the d-orbitals of transition metals [20–22]. For both functionals, the Grimme D3 dispersion correction was applied with the Becke–Johnson damping function [23,24] to account for dispersion interactions.

Cluster calculations were performed using the program package TURBOMOLE with finite-sized clusters terminated with H-atoms [25,26]. Geometry optimizations were performed with the def2-SVP basis while a larger def2-TZVP basis was applied for single-point calculations [27]. Electronic steps were converged to 10^{-6} a.u. in the total energy and 10^{-3} a.u. in the orbital energies, while geometric steps were converged to 10^{-3} a.u. in the maximum norm of the Cartesian gradient. Each cluster was calculated with various preassigned multiplicities until the most stable spin state was found and determined as the ground state. Atomic charges were obtained with the natural bond orbital (NBO) population analysis [28] and abbreviated as NBO charges.

Periodic calculations were performed with the Vienna Ab initio Simulation Package (VASP) using the projector augmented-wave (PAW) method with an energy cutoff $E_{cut} = 600$ eV [29–32]. The RMM-DIIS algorithm was applied for electronic relaxation and the electronic convergence criterion was set to 10^{-5} eV. The Gaussian smearing approach with a smearing width of $\sigma = 0.05$ eV was applied. K-points were sampled using a $3 \times 3 \times 1$ Γ-centered mesh grid for the geometry optimization and $6 \times 6 \times 1$ grid for single-point calculations. Ionic relaxation steps were performed with the conjugate gradient algorithm with a force convergence of $10^{-2} \frac{eV}{\text{Å}}$. During geometry optimization, all atomic positions and lattice constants were relaxed under the constraint of constant unit cell volume (ISIF = 4), with an initial vacuum width of 15 Å perpendicular to the 2D material. All atomic structures were visualized with VESTA [33].

3. Results and Discussion

3.1. Structural Model Comparison

For the purpose of the comparison between pyrrolic and pyridinic MN_4 sites embedded in a graphene layer, we constructed several clusters and unit cell models of different shapes and sizes as shown in Figure 1. Extending a basic pyrrolic MN_4C_{20} unit with purely

hexagonal carbon rings generally led to huge distortions in the planarity of the cluster, indicative of a high lattice strain in an extended environment. In order to minimize the lattice strain and keep the clusters planar, seven-membered rings were introduced next to the pyrrole units.
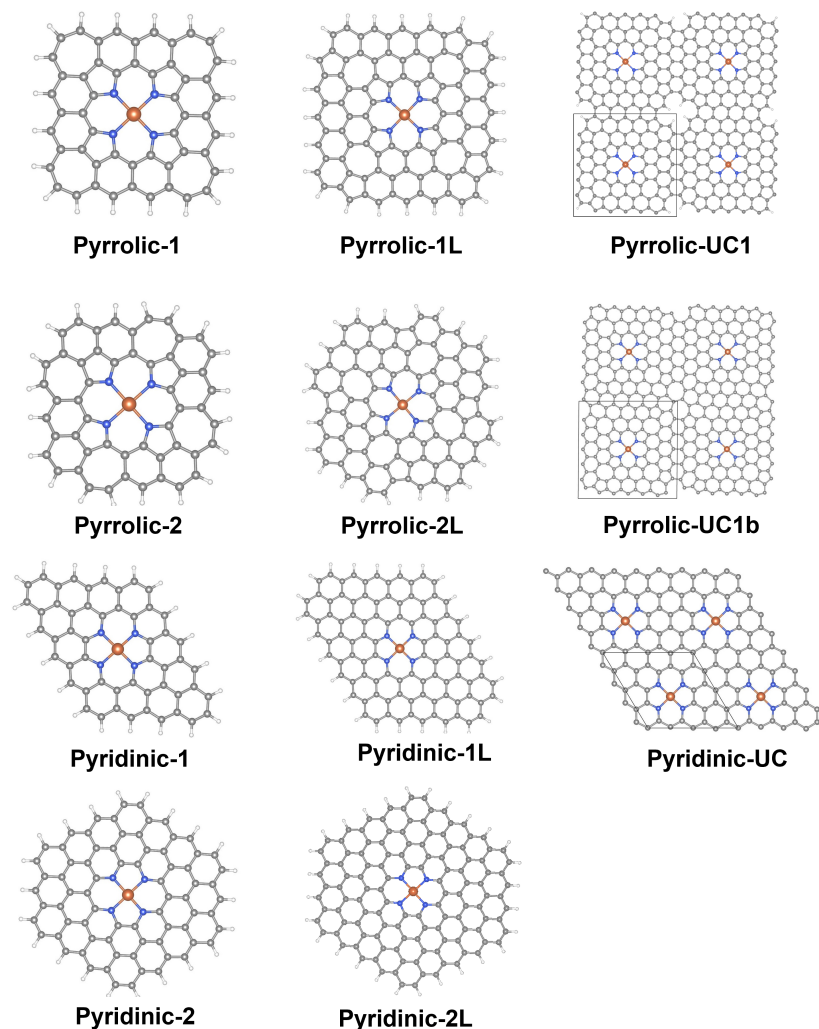
Pyrrolic-1   **Pyrrolic-1L**   **Pyrrolic-UC1**

Pyrrolic-2   **Pyrrolic-2L**   **Pyrrolic-UC1b**

Pyridinic-1   **Pyridinic-1L**   **Pyridinic-UC**

Pyridinic-2   **Pyridinic-2L**

Figure 1. Structural models used for the comparison of binding energies and bond lengths in Table 1, including small cluster models (**left**), corresponding larger cluster models (**middle**), and unit cell models (**right**).

Considering the success of the Zn-Fe transmetallation strategy in producing Fe-N-Cs with high dopant concentrations [8,16], Zn and Fe are ideal candidates as reference for constructing the model used in the DFT calculations. Based on the NBO charges (Table 2) and frontier molecular orbital (FMO) analysis (Figures S3–S6 in Supplementary Materials), Zn and Fe represent two different types of binding in the N_4 site, with Zn exhibiting highly ionic binding character while Fe contains covalent contributions from the d-orbitals. In constructing a cluster model, the finite-size of the π-system compared to an extended graphene can potentially influence its chemical properties. We thus studied the binding of Fe and Zn in the N_4 sites of different shapes and sizes and compared them to a periodic model (Table 1). The binding energy of species M is defined as

$$E_b = E_{MN_4} - E_{N_4} - E_M \tag{1}$$

where E_{N_4} and E_M are the charge-neutral DFT ground state energies of the empty N_4 site and the metal atom, respectively. For the cluster models, a plot of the binding energies

against the M-N bond lengths is shown in Figure 2. Due to the additional inner-shell carbon atoms, the pyrrolic MN_4C_{12} sites were larger than the pyridinic MN_4C_{10} sites. In addition, the size of the pyrrolic N_4 site was further influenced by the arrangement of carbon atoms surrounding the MN_4 unit, with the pyrrolic-2(L) motifs exhibiting longer bond lengths than pyrrolic-1(L). We first examined the deviations between values obtained from the cluster model and periodic model (pyrrolic-1/1L/UC1 and pyridinic-1/1L/UC1). Fortunately, considering methodological differences in the basis set, pseudopotentials, and extensiveness of the models, only slight differences between the cluster and the unit cell models were observed. For Fe, the smaller pyrrolic-1 and pyridinic-1 cluster had a deviation of up to 0.23 eV compared to the unit cell model, but the larger clusters (pyrrolic-1L, pyridinic-1L) almost exactly reproduced the binding energies and bond lengths of the respective unit cell models (pyrrolic-UC1, pyridinic-UC). For Zn, the cluster models consistently predicted a stronger binding than the unit cell model for both pyrrolic and pyridinic models. Surprisingly, it was the pyridinic motif that deviated relatively strongly between the cluster model and unit cell model. The reason for the deviation seems to lie in the geometric distortion of the Zn-N bond lengths to compensate for the unfavorably short Zn-N bond lengths at pyridinic sites which only occurred on the pyridinic-1(L) clusters where the D_{2h} symmetry of the pyridinic ZnN_4 site was not retained.

Table 1. M-N bond lengths and binding energies of Fe and Zn in various N_4 models obtained with PBE-D3(BJ) functional.

Species	Model	E_b (eV)	d_{M-N} (Å)
	Pyrrolic-1	−9.64	1.95
	Pyrrolic-1L	−9.89	1.95
	Pyrrolic-UC1	−9.87	1.95
	Pyrrolic-UC1b	−10.11	1.93, 1.96
	Pyrrolic-2	−8.53	1.97
Fe	Pyrrolic-2L	−9.45	2.00
	Pyridinic-1	−7.86	1.90, 1.91
	Pyridinic-1L	−7.77	1.90, 1.91
	Pyridinic-UC	−7.74	1.89
	Pyridinic-2	−7.57	1.90
	Pyridinic-2L	−7.36	1.90
	Pyrrolic-1	−6.01	2.02
	Pyrrolic-1L	−6.15	2.03
	Pyrrolic-UC1	−5.94	2.02
	Pyrrolic-UC1b	−6.11	1.99, 2.03
	Pyrrolic-2	−5.43	2.06
Zn	Pyrrolic-2L	−6.34	2.06
	Pyridinic-1	−4.14	1.96, 2.00
	Pyridinic-1L	−4.11	1.96, 1.99
	Pyridinic-UC	−3.79	1.96
	Pyridinic-2	−3.92	1.97
	Pyridinic-2L	−3.62	1.97

Another important aspect to consider when constructing clusters to model N_4 embedded in graphene is the shape of the cluster, as influences arising from the boundary carbons should be avoided when describing catalytic activity at the MN_4 site. We thus compared two different pyrrolic clusters with different placement of the seven-membered rings (pyrrolic-1,2) as well as their respective extension of the carbon backbone (pyrrolic-1L,2L). The pyrrolic-2 model exhibited a large deviation of about 1 eV in the binding energy compared to the pyrrolic-1 and pyrrolic-UC values in Table 1. The anomaly can be explained by the saddle-like curvature of the pyrrolic-2 model in contrast to the other planar pyrrolic models. Increasing the size of the pyrrolic-2 cluster reduced the deviation as the cluster became more planar. Nevertheless, some deviations still remained due to the inherently

larger size of the N_4 cavity in the pyrrolic-2L model along with a slight residual curvature. For the pyridinic model, a cluster model with a different shape was constructed to examine the influence of the cluster shape (pyridinic-2, pyridinic-2L). Due to these models retaining the D_{2h} symmetry of the MN_4 site, the geometric distortion apparent in the pyridinic-1(L) clusters was not observed, and the respective binding energies were closer to that of the unit cell. However, these models seemed to underestimate the binding strength of Fe in pyridinic N_4 sites, especially the pyridinic-2L cluster with a deviation of 0.4 eV to the unit cell model.
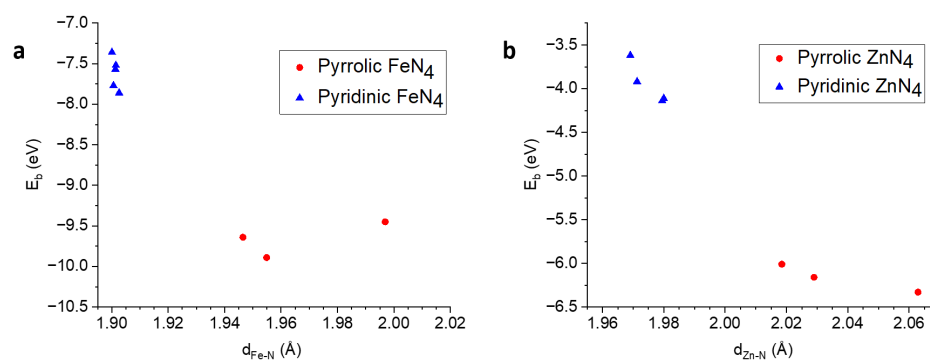

Figure 2. Plot of binding energy E_b against M-N bond length d_{M-N} for (**a**) Fe and (**b**) Zn in respective clusters.

For the pyrrolic MN_4 unit cell, an alternative model was constructed whereby the four hydrogen atoms at the unit cell boundary of the pyrrolic-UC1 model were replaced by two carbon atoms, producing a cavity-free carbon lattice (pyrrolic-UC1b). The closing of the lattice in this manner led to some ring strain in the system, evident in the presence of some distorted hexagons along the unit cell boundary (Figure 1). As a result, the breaking of the unit cell symmetry could even be observed in the inequivalent M-N bond lengths of the pyrrolic-UC1b model and the binding energies obtained (Fe: -10.11 eV; Zn: -6.11 eV) were slightly higher in magnitude than the pyrrolic-UC1 model (Fe: -9.87 eV; Zn: -5.94 eV). Due to the presence of ring strain, the pyrrolic-UC1b model may not be suitable for reaction studies as the introduction of adsorbates can produce incomparable structures in attempts to relieve the ring strains. However, since the energy deviations were relatively small at 0.2 eV (<3% of the calculated binding energies), we do not expect significant anomalies in the intrinsic chemical properties of the MN_4 sites. Furthermore, since the pyrrolic-UC1 model contains a cavity which introduces an artificial band gap in the system, the pyrrolic-UC1b model would be better suited for studying the electrical and electronic properties in an extended system, including band gaps, Fermi energies and conductivities.

Finally, we examined the relationship between the M-N bond length and the binding energy for planar models (i.e., excluding pyrrolic-2). From Figure 2b, it can be observed that the binding energy of Zn has a strong dependence on the size of the N_4 cavity with a longer Zn-N bond length generally corresponding to a stronger binding. It is thus evident that Zn has a higher affinity towards larger cavities, possibly explaining the dominance of pyrrolic ZnN_4 site observed when Zn was introduced during pyrolysis [8]. The geometric distortion observed in the unequal Zn-N bond lengths (Table 1) leading to a stronger Zn binding in the pyridinic-1(L) clusters was further evidence that the small pyridinic motifs were not ideal for Zn. In contrast, Fe exhibited highly consistent bond lengths around 1.90 Å among the pyridinic motifs and much smaller distortion at the pyridinic-1(L) site, hinting towards its geometric affinity for the smaller pyridinic site. The relative affinity of each metal towards pyrrolic and pyridinic MN_4 sites is further discussed in Section 3.2.3.

3.2. Binding of Metals in N_4

　　In order to identify possible candidates for templating and substitution, we studied the binding of metals from the first three periods of the periodic table in the pyrrolic and pyridinic N_4 pockets. Table 2 displays information on the binding of various metals in the pyrrolic N_4 sites. In order to reduce the effects of the delocalization errors associated with the GGA functionals, we used the hybrid PBE0 functional in this study. The binding energies and M-N bond lengths shown in Table 2 can be compared with those in Table 1 to illustrate the differences between PBE and PBE0. It was observed that the inclusion of a 25% exact exchange in the PBE0 functional led to a weakening of the binding energy of Fe by 0.5–0.8 eV while the Zn binding was strengthened by 0.3–1.2 eV. The difference in behavior could be explained by the degree of ionic and covalent binding characters within the MN_4 sites. The NBO charge of Zn was very close to +2, suggesting an almost fully ionic binding character in the formally N_4^{2-} pocket. Contrastingly, Fe and many other transition metals exhibited NBO charges that were significantly smaller than +2, implying electron donation from the π-system to Fe and thus a certain extent of covalent binding character involving electron delocalization. Evidently, the delocalization error associated with the GGA functionals favored the latter binding situation (with additional delocalization of the d-electrons with the π-system) and thus overestimated the binding strength in these cases, whereas ionic binding strengths were conversely underestimated. The advantage of using cluster models is highlighted here, since the implementation of hybrid functionals in periodic calculations can be computationally expensive, especially for pyrrolic MN_4 motifs which require relatively large unit cells due to the defects in the carbon lattice.

Table 2. Binding energies E_b obtained with Equation (1), M-N bond length d_{M-N}, NBO charge of metal Q_M in the pyrrolic-1 and pyridinic-1 clusters and the energy difference between the pyrrolic-1 and pyridinic-1 isomers ΔE_{isomer} obtained with Equation (3). The geometry was optimized with PBE0-D3(BJ)/def2-SVP, followed by a single-point calculation with PBE0-D3(BJ)/def2-TZVP to obtain energies and charges. Species that are not coplanar to both N_4 pocket are marked with *, while species that are not coplanar only with the pyridinic motif are marked with *^{pyri}. Nonplanar binding motifs are shown in Figures S1 and S2 of the Supplementary Materials.

Metal	E_b (eV)		d_{M-N} (Å)		Q_M (e)		ΔE_{isomer}
	Pyrrolic	Pyridinic	Pyrrolic	Pyridinic	Pyrrolic	Pyridinic	(eV)
empty	-	-	2.01 **	1.92 **	-	-	6.19
Li	−7.27	−5.31	2.00	1.94	+0.86	+0.86	4.23
Na *	−5.66	−3.49	2.25	2.27	+0.91	+0.93	4.03
K *	−5.14	−3.16	2.63	2.66	+0.95	+0.97	4.21
Be	−10.31	−8.35	1.91	1.84	+1.67	+1.67	4.24
Mg	−9.13	−6.09	2.02	1.97	+1.78	+1.77	3.15
Ca *	−9.25	−6.20	2.28	2.27	+1.79	+1.78	3.15
Sc *	−12.51	−8.51	2.08	2.08	+2.02	+1.89	2.19
Ti *^{pyri}	−12.15	−8.04	2.01	2.02	+1.68	+1.59	2.09
V *^{pyri}	−11.18	−7.61	1.99	1.99	+1.45	+1.22	2.62
Cr	−10.02	−6.84	2.00	1.96	+1.20	+1.14	3.02
Mn	−9.35	−5.97	1.96	1.94	+1.58	+1.24	2.81
Fe	−9.12	−7.05	1.96	1.91	+1.18	+1.09	4.12
Co	−9.61	−7.33	1.95	1.90	+1.08	+1.07	3.92
Ni	−9.49	−7.24	1.95	1.88	+1.03	+0.97	3.94
Cu	−7.95	−5.47	1.98	1.93	+1.35	+1.31	3.71
Zn	−7.17	−4.40	2.01	1.97	+1.66	+1.64	3.42
Al	−11.89	−8.46	1.94	1.89	+1.97	+1.88	2.76
Ga	−9.45	−6.03	1.97	1.93	+1.88	+1.79	2.78

*: not planar in pyrrolic and pyridinic MN_4 ; *^{pyri}: not planar in pyridinic MN_4; **: fictitious bond length taken as half the diagonal N-N distance.

3.2.1. Binding Geometry

In Table 2, metal atoms marked with * and *^{pyri} are not coplanar with the nitrogen atoms in which the perpendicular distances from M to the N$_4$ plane were measured to be greater than 0.2 Å. Their relatively long M-N bond lengths suggest that they were too large to fit into the respective N$_4$ site. Interestingly, the longest M-N bond length among the planar MN$_4$ sites were generally exhibited by Mg and Zn, two of the most commonly used templating agents [8,14,16,17]. It is further noteworthy that the M-N bond lengths of these metals closely matched the size of the relaxed metal-free pyrrolic-1 cluster, suggesting excellent geometric fit to the pyrrolic motifs. Contrastingly, mid-to-late transition metals (Mn-Cu) and group 13 metals bound in the pyridinic motifs were shown to fit geometrically to the naturally smaller pyridinic-1 sites. Comparing the optimized geometries of the first-row transition metals in the N$_4$ sites, it can be observed that most first-row transition metals remained bound within the N$_4$ site with the exception of early transition metals (Sc, Ti, and V). Ti and V were particularly unique as they fitted into the pyrrolic MN$_4$ clusters, but were slightly displaced from the pyridinic one, suggesting a relatively high geometric affinity to the pyrrolic motif.

3.2.2. Binding Energy

The binding energies shown in Table 2 were calculated with Equation (1). In the framework of the transmetallation strategy, we could identify metals with smaller binding energies as ideal templating agents that could be substituted with relative ease. Transmetallation should then be carried out using species with a stronger binding energy.

Among the main-group elements, there was a clear trend between the strength of the binding and the valency of the metals (group 1 < group 2 < group 13). The increasing strength of the ionic binding was also reflected in the increasing NBO charges. Nevertheless, we further observed that the NBO charge of group-13 metals and early transition metals were closer to +2 despite their preference for an oxidation state of +3, indicating that the N$_4^{2-}$ site could not be further reduced. The mismatch in the oxidation state suggests that these metals would be readily oxidized and possibly poisoned by anionic ligands.

Due to the varying participation of d-orbitals and preferences for oxidation states among the first-row transition metals, their corresponding binding energies spanned a wide range from −7.17 eV for Zn to −12.51 eV for Sc. The progression of the binding energy and NBO charge across the first-row transition metals are illustrated in Figure 3a,b. Among the early transition metals (Sc–Cr), the binding became weaker with an increasing atomic number accompanied by a decreasing NBO charge. This trend reflected the increasing electronegativity and thus ionization energy of the transition metals with an increasing atomic number, leading to weaker ionic interactions and thus smaller binding energies. It is also noteworthy that the trend-breaking low electronegativity of Mn in the Pauling electronegativity scale was reproduced in the calculated NBO charges. Compared to the early transition metals, the late transition metals (Fe–Zn) showed a contradicting trend whereby an increase in NBO charge was instead correlated to a weaker binding. We attribute this deviation to the covalent contribution which arises from the relatively high electronegativities of the late transition metals, especially Fe, Co, and Ni. As the NBO charges deviated significantly from the expected oxidation state of +2, there was some electron donation from the π-system into the d-orbitals of the transition metals. This was further confirmed by a FMO analysis from which orbitals indicating π-d interactions were observed in the FeN$_4$ but not in the ZnN$_4$ clusters (Figures S3–S6 of Supplementary Materials). We quantified the degree of electron donation $n_{\pi \to d}$ by comparing the net NBO population of the d-orbitals with the expected occupancy of an M^{2+} ion (e.g., d^6 for Fe^{2+}).

$$n_{\pi \to d} = n_d - (Z - 20) \qquad (2)$$

where n_d is the d-orbital population obtained with the NBO population analysis, and $(Z - 20)$ is the expected d-orbital population for a first-row transition metal with nuclear

charge Z in the oxidation state of +2. The separation in trends between the early and late transition metal is reproduced in Figure 3c,d, whereby late transition metals Fe-Zn exhibited a positive correlation between the $\pi \rightarrow d$ electron transfer and the magnitude of the binding energy. This further confirmed that the deviation of the NBO charge from the ideal oxidation state of +2 for transition metals originated from the electron-accepting properties of the d-orbitals. From Ni to Zn, as the availability of unoccupied d-orbitals decayed to 0, a sharp decrease in binding strength was also observed. As a result of its relatively high electronegativity and lack of unoccupied d-orbitals for accepting electrons, Zn exhibited the weakest binding energy among the elements studied and is thus an ideal candidate for subsequent substitution in a templating synthesis strategy.
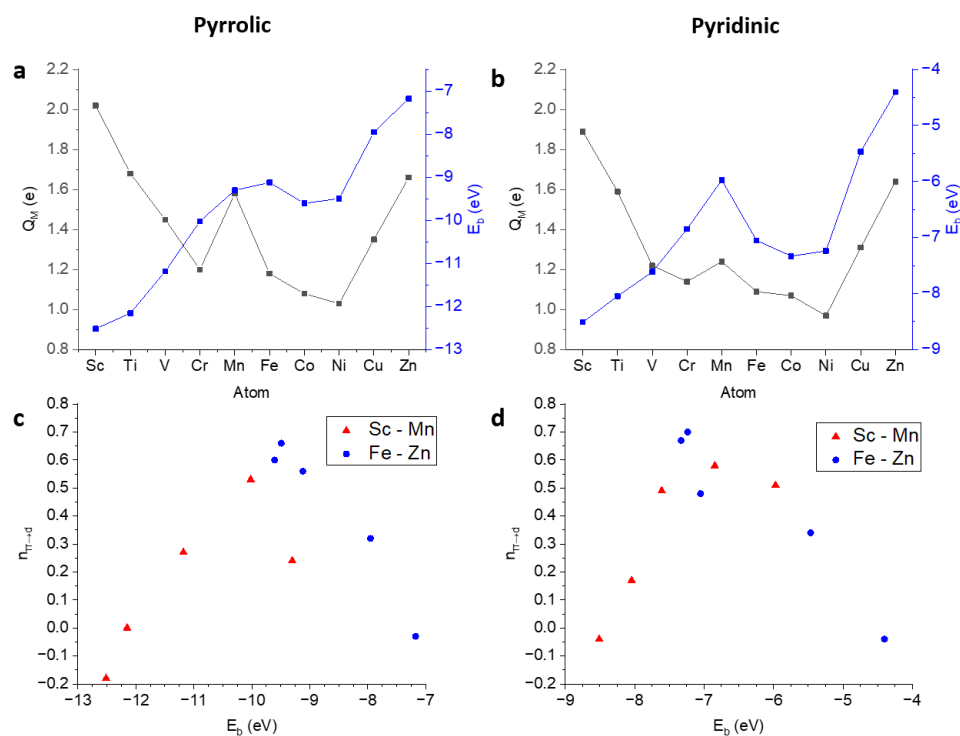

Figure 3. NBO charge (black) and corresponding binding energies (blue) of first-row transition metals in (**a**) pyrrolic-1 and (**b**) pyridinic-1 clusters. Plot of net $\pi \rightarrow d$ electron transfer against metal binding energies for (**c**) pyrrolic-1 and (**d**) pyridinic-1 clusters.

3.2.3. Affinity towards Pyrrolic Motifs

Since the pyrrolic-1 and pyridinic-1 clusters are isomers, the difference in total energy ΔE_{isomer} shown in Table 2 provides insights on the respective metals' affinity towards pyrrolic and pyridinic MN_4 motifs. The energy difference between isomeric pyrrolic-1 and pyridinic-1 MN_4 cluster is obtained with

$$\Delta E_{\text{isomer}} = E_{\text{pyrrolic-1}} - E_{\text{pyridinic-1}} \tag{3}$$

where $E_{\text{pyrrolic-1}}$ and $E_{\text{pyridinic-1}}$ are the total electronic energies of metal-bound pyrrolic-1 and pyridinic-1 clusters, respectively. From this definition, the lower the ΔE_{isomer}, the higher its affinity towards pyrrolic MN_4 motifs. In general, due to the presence of defects, pyrrolic motifs are still thermodynamically less stable than pyridinic motifs. However, since it has been proven that Zn forms pyrrolic MN_4 motifs [8] and several recent studies have independently arrived to the conclusion that it is the pyrrolic MN_4 sites that are responsible for the high ORR activity of Fe-N-Cs [10,11] as well as the CO_2RR activity of Ni-N-Cs [12], it is clear that thermodynamics is not the deciding factor on the type of MN_4 sites that are formed during pyrolysis. In addition, it is also worthy to note that Sc,

Ti, and V exhibited some of the smallest ΔE_{isomer} due to significant geometry differences between the pyrrolic and pyridinic MN_4 clusters as discussed in Section 3.2.1.

Since Zn is known to form pyrrolic motifs, metals with lower ΔE_{isomer} than Zn are also likely to do so. Referring to the values shown in Table 2 and Figure 4, the affinity of Zn towards pyrrolic motifs was actually relatively high compared with many other metals, including group-2 metals (Mg, Ca), group-13 metals (Al, Ga) as well as early transition metals (Sc, Ti, V, Cr, Mn). According to Figure 4a, a general negative trend could be observed between the ΔE_{isomer} and the average NBO charge, further confirming that the pyrrolic motif has a higher preference towards ionic binding than the pyridinic motif. Conversely, late-transition metals which formed covalent binding with the π-system (Fe-Cu) had higher ΔE_{isomer} and thus a lower affinity towards forming pyrrolic motifs. This difference in affinity towards ionic and covalent binding further explains an anomaly of Mn, in which two very different binding characters were observed in the pyrrolic and pyridinic motifs. Highly ionic binding was preferred for pyrrolic MnN_4 with a large NBO charge (+1.58 e) whereas indications of $\pi \rightarrow d$ donation were reflected in the significantly lower NBO charge in pyridinic MnN_4 (+1.24 e).
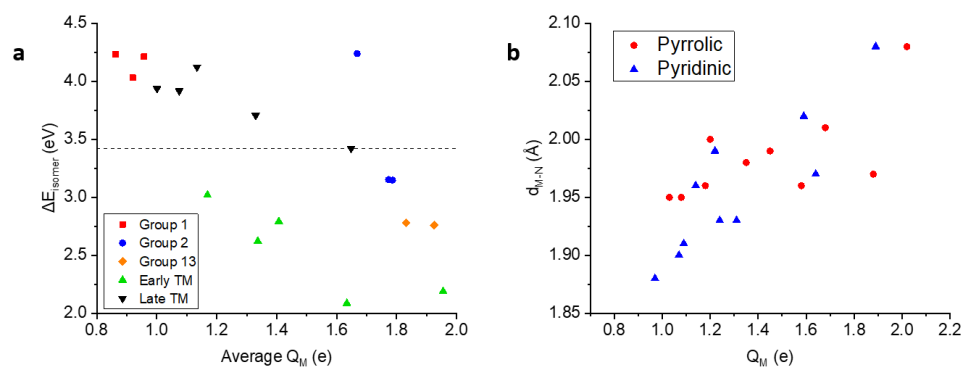

Figure 4. (**a**) Plot of ΔE_{isomer} against the average NBO charge of metal M in pyrrolic and pyridinic N_4 sites. The ΔE_{isomer} for Zn is marked with a dashed line. (**b**) Plot of M-N distance against the NBO charge of transition metal M.

Coincidentally, the direct synthesis of M-N-Cs containing late transition metals, especially Fe, Co, and Ni, generally face challenges involving graphitization and inorganic side phases [12,18,34,35]. A possible explanation for their graphitization tendency could be their higher affinity towards pyridinic motifs which exhibit a closer structural resemblance to graphene due to the absence of defective carbon rings. Conversely, the structural defects in the carbon lattice of pyrrolic MN_4 can be crucial in preventing graphitization as significant carbon rearrangement involving the breaking and formation of multiple C-C bonds is required to recover the honeycomb graphite structure. Thus, although Zn has the weakest binding energy and is thus possibly the easiest to remove for a transmetallation strategy, other metals such as Mg and early transition metals have a higher affinity towards pyrrolic motifs, which can be optimal for their survivability in the graphene lattice, possibly leading to higher single-atomic dopant concentrations. Nevertheless, removing these metals from the N_4 sites is likely to require harsher transmetallation conditions due to their stronger binding energies.

4. Conclusions

In conclusion, we constructed and compared several cluster models of pyrrolic and pyridinic MN_4 sites based on the binding energy and geometry of Zn and Fe. Zn was shown to bind stronger on larger N_4 sites and thus had a higher preference towards pyrrolic motifs in contrast to Fe, which had a higher preference for smaller N_4 sites. The study was further extended to other metals and it was shown based on binding energies, M-N bond lengths, and an NBO charge analysis that the pyrrolic N_4 site is ideal for ionic binding of

main-group metals and early transition metals, while the smaller pyridinic N_4 site is more suitable for covalent binding, especially of late-transition metals, where $\pi \rightarrow$ d electron donation plays a significant role in binding. Knowledge of the metals' affinity towards the types and sizes of the N_4 site, as well as their binding strength relative to other metals, is likely to be critical in formulating a templating strategy for synthesizing carbon materials with the desired MN_4 motifs.

Supplementary Materials: The following supporting information can be downloaded at: https://www.mdpi.com/article/10.3390/catal13030566/s1, atomics coordinates for structural models containing Fe; Figures S1 and S2: top and side-view of non-planar MN_4 sites in pyrrolic-1 and pyridinic-1 clusters; Figures S3–S6: frontier molecular orbital diagram of FeN_4 and ZnN_4 in the pyrrolic-1 and pyridinic-1 clusters obtained with the program Molden [36,37].

Author Contributions: Conceptualization, J.L.L.; methodology, J.L.L.; validation, J.L.L. and B.P.; formal analysis, J.L.L.; investigation, J.L.L.; resources, J.L.L. and B.P.; data curation, J.L.L.; writing —original draft preparation, J.L.L.; writing—review and editing, J.L.L. and B.P.; visualization, J.L.L.; supervision, B.P.; project administration, B.P.; funding acquisition, J.L.L. and B.P. All authors have read and agreed to the published version of the manuscript.

Data Availability Statement: See Supplementary Materials. Further data can be requested from the authors.

Conflicts of Interest: The authors declare no conflict of interest.

Abbreviations

The following abbreviations are used in this manuscript:

M-N-Cs	Metal- and nitrogen-doped carbons
ORR	Oxygen reduction reaction
CO_2RR	CO_2 reduction reaction
DFT	Density functional theory
GGA	Generalized gradient approximation
RMM-DIIS	Residual minimization–direct inversion in the iterative subspace
NBO	Natural bond orbital
FMO	Frontier molecular orbitals

References

1. Gasteiger, H.A.; Kocha, S.S.; Sompalli, B.; Wagner, F.T. Activity benchmarks and requirements for Pt, Pt-alloy, and non-Pt oxygen reduction catalysts for PEMFCs. *Appl. Catal. B Environ.* **2005**, *56*, 9–35. [CrossRef]
2. Shao, M.; Chang, Q.; Dodelet, J.P.; Chenitz, R. Recent advances in electrocatalysts for oxygen reduction reaction. *Chem. Rev.* **2016**, *116*, 3594–3657. [CrossRef] [PubMed]
3. Hori, Y. Electrochemical CO2 reduction on metal electrodes. *Mod. Asp. Electrochem.* **2008**, 89–189. [CrossRef]
4. Kortlever, R.; Shen, J.; Schouten, K.J.P.; Calle-Vallejo, F.; Koper, M.T. Catalysts and reaction pathways for the electrochemical reduction of carbon dioxide. *J. Phys. Chem. Lett.* **2015**, *6*, 4073–4082. [CrossRef]
5. Lefèvre, M.; Proietti, E.; Jaouen, F.; Dodelet, J.P. Iron-based catalysts with improved oxygen reduction activity in polymer electrolyte fuel cells. *Science* **2009**, *324*, 71–74. [CrossRef]
6. Wang, Y.; Cui, X.; Peng, L.; Li, L.; Qiao, J.; Huang, H.; Shi, J. Metal–nitrogen–carbon catalysts of specifically coordinated configurations toward typical electrochemical redox reactions. *Adv. Mater.* **2021**, *33*, 2100997. [CrossRef]
7. Jaouen, F.; Jones, D.; Coutard, N.; Artero, V.; Strasser, P.; Kucernak, A. Toward platinum group metal-free catalysts for hydrogen/air proton-exchange membrane fuel cells. *Johns. Matthey Technol. Rev.* **2018**, *62*, 231–255. [CrossRef]
8. Menga, D.; Low, J.L.; Li, Y.S.; Arčon, I.; Koyutürk, B.; Wagner, F.; Ruiz-Zepeda, F.; Gaberšček, M.; Paulus, B.; Fellinger, T.P. Resolving the dilemma of Fe–N–C catalysts by the selective synthesis of tetrapyrrolic active sites via an imprinting strategy. *J. Am. Chem. Soc.* **2021**, *143*, 18010–18019. [CrossRef]

9. Zitolo, A.; Goellner, V.; Armel, V.; Sougrati, M.T.; Mineva, T.; Stievano, L.; Fonda, E.; Jaouen, F. Identification of catalytic sites for oxygen reduction in iron-and nitrogen-doped graphene materials. *Nat. Mater.* **2015**, *14*, 937–942. [CrossRef]

10. Ni, L.; Gallenkamp, C.; Wagner, S.; Bill, E.; Krewald, V.; Kramm, U.I. Identification of the catalytically dominant iron environment in iron-and nitrogen-doped carbon catalysts for the oxygen reduction reaction. *J. Am. Chem. Soc.* **2022**, *144*, 16827–16840. [CrossRef]

11. Hu, X.; Chen, S.; Chen, L.; Tian, Y.; Yao, S.; Lu, Z.; Zhang, X.; Zhou, Z. What is the Real Origin of the Activity of Fe–N–C Electrocatalysts in the O2 Reduction Reaction? Critical Roles of Coordinating Pyrrolic N and Axially Adsorbing Species. *J. Am. Chem. Soc.* **2022**, *144*, 18144–18152. [CrossRef]

12. Koshy, D.M.; Chen, S.; Lee, D.U.; Stevens, M.B.; Abdellah, A.M.; Dull, S.M.; Chen, G.; Nordlund, D.; Gallo, A.; Hahn, C.; et al. Understanding the origin of highly selective CO2 electroreduction to CO on Ni, N-doped carbon catalysts. *Angew. Chem. Int. Ed.* **2020**, *59*, 4043–4050. [CrossRef] [PubMed]

13. Zhang, N.; Zhou, T.; Chen, M.; Feng, H.; Yuan, R.; Yan, W.; Tian, Y.; Wu, X.; Chu, W.; Wu, C.; et al. High-purity pyrrole-type FeN 4 sites as a superior oxygen reduction electrocatalyst. *Energy Environ. Sci.* **2020**, *13*, 111–118. [CrossRef]

14. Menga, D.; Ruiz-Zepeda, F.; Moriau, L.; Šala, M.; Wagner, F.; Koyutürk, B.; Bele, M.; Petek, U.; Hodnik, N.; Gaberšček, M.; et al. Active-site imprinting: Preparation of Fe–N–C catalysts from zinc ion–templated ionothermal nitrogen-doped carbons. *Adv. Energy Mater.* **2019**, *9*, 1902412. [CrossRef]

15. Jiao, L.; Li, J.; Richard, L.L.; Sun, Q.; Stracensky, T.; Liu, E.; Sougrati, M.T.; Zhao, Z.; Yang, F.; Zhong, S.; et al. Chemical vapour deposition of Fe–N–C oxygen reduction catalysts with full utilization of dense Fe-N4 sites. *Nat. Mater.* **2021**, *20*, 1385–1391. [CrossRef] [PubMed]

16. Mehmood, A.; Gong, M.; Jaouen, F.; Roy, A.; Zitolo, A.; Khan, A.; Sougrati, M.T.; Primbs, M.; Bonastre, A.M.; Fongalland, D.; et al. High loading of single atomic iron sites in Fe–NC oxygen reduction catalysts for proton exchange membrane fuel cells. *Nat. Catal.* **2022**, *5*, 311–323. [CrossRef]

17. Mehmood, A.; Pampel, J.; Ali, G.; Ha, H.Y.; Ruiz-Zepeda, F.; Fellinger, T.P. Facile metal coordination of active site imprinted nitrogen doped carbons for the conservative preparation of non-noble metal oxygen reduction electrocatalysts. *Adv. Energy Mater.* **2018**, *8*, 1701771. [CrossRef]

18. Fellinger, T.P.; Menga, D.; Buzanich, A.G.; Wagner, F. Evaluation of the Specific Activity of M-N-Cs and the Intrinsic Activity of Tetrapyrrolic Fe-N4 Sites for the Oxygen Reduction Reaction. *Angew. Chem.* **2022**, e202207089.

19. Perdew, J.P.; Burke, K.; Ernzerhof, M. Generalized gradient approximation made simple. *Phys. Rev. Lett.* **1996**, *77*, 3865. [CrossRef]

20. Perdew, J.P.; Ernzerhof, M.; Burke, K. Rationale for mixing exact exchange with density functional approximations. *J. Chem. Phys.* **1996**, *105*, 9982–9985. [CrossRef]

21. Ernzerhof, M.; Scuseria, G.E. Assessment of the Perdew–Burke–Ernzerhof exchange-correlation functional. *J. Chem. Phys.* **1999**, *110*, 5029–5036. [CrossRef]

22. Tolba, S.A.; Gameel, K.M.; Ali, B.A.; Almossalami, H.A.; Allam, N.K. The DFT+U: Approaches, Accuracy, and Applications. In *Density Functional Calculations*; Yang, G., Ed.; IntechOpen: Rijeka, Croatia, 2018; Chapter 1. [CrossRef]

23. Grimme, S.; Antony, J.; Ehrlich, S.; Krieg, H. A consistent and accurate ab initio parametrization of density functional dispersion correction (DFT-D) for the 94 elements H-Pu. *J. Chem. Phys.* **2010**, *132*, 154104. [CrossRef] [PubMed]

24. Grimme, S.; Ehrlich, S.; Goerigk, L. Effect of the damping function in dispersion corrected density functional theory. *J. Comput. Chem.* **2011**, *32*, 1456–1465. [CrossRef] [PubMed]

25. Ahlrichs, R.; Bär, M.; Häser, M.; Horn, H.; Kölmel, C. Electronic structure calculations on workstation computers: The program system turbomole. *Chem. Phys. Lett.* **1989**, *162*, 165–169. [CrossRef]

26. Khosravi, A.; Vessally, E.; Oftadeh, M.; Behjatmanesh-Ardakani, R. Ammonia capture by MN4 (M= Fe and Ni) clusters embedded in graphene. *J. Coord. Chem.* **2018**, *71*, 3476–3486. [CrossRef]

27. Weigend, F.; Ahlrichs, R. Balanced basis sets of split valence, triple zeta valence and quadruple zeta valence quality for H to Rn: Design and assessment of accuracy. *Phys. Chem. Chem. Phys.* **2005**, *7*, 3297–3305. [CrossRef]

28. Reed, A.E.; Weinstock, R.B.; Weinhold, F. Natural population analysis. *J. Chem. Phys.* **1985**, *83*, 735–746. [CrossRef]

29. Kresse, G.; Hafner, J. Ab initio molecular dynamics for liquid metals. *Phys. Rev. B* **1993**, *47*, 558. [CrossRef] [PubMed]

30. Kresse, G.; Furthmüller, J. Efficiency of ab-initio total energy calculations for metals and semiconductors using a plane-wave basis set. *Comput. Mater. Sci.* **1996**, *6*, 15–50. [CrossRef]

31. Kresse, G.; Furthmüller, J. Efficient iterative schemes for ab initio total-energy calculations using a plane-wave basis set. *Phys. Rev. B* **1996**, *54*, 11169. [CrossRef]

32. Kresse, G.; Joubert, D. From ultrasoft pseudopotentials to the projector augmented-wave method. *Phys. Rev. B* **1999**, *59*, 1758. [CrossRef]

33. Momma, K.; Izumi, F. VESTA 3 for three-dimensional visualization of crystal, volumetric and morphology data. *J. Appl. Crystallogr.* **2011**, *44*, 1272–1276. [CrossRef]

34. Iwase, K.; Ebner, K.; Diercks, J.S.; Saveleva, V.A.; Unsal, S.; Krumeich, F.; Harada, T.; Honma, I.; Nakanishi, S.; Kamiya, K.; et al. Effect of cobalt speciation and the graphitization of the carbon matrix on the CO2 electroreduction activity of Co/N-doped carbon materials. *ACS Appl. Mater. Interfaces* **2021**, *13*, 15122–15131. [CrossRef] [PubMed]

35. Yudasaka, M.; Kikuchi, R. Graphitization of carbonaceous materials by Ni, Co and Fe. In *Supercarbon*; Springer: Berlin/Heidelberg, Germany, 1998; pp. 99–105.

36. Schaftenaar, G.; Noordik, J.H. Molden: A pre-and post-processing program for molecular and electronic structures. *J. Comput. Aided Mol. Des.* **2000**, *14*, 123–134. [CrossRef] [PubMed]
37. Schaftenaar, G.; Vlieg, E.; Vriend, G. Molden 2.0: Quantum chemistry meets proteins. *J. Comput. Aided Mol. Des.* **2017**, *31*, 789–800.